Vesicouretal reflux in children: A phantom study of microwave heating and radiometric thermometry of pediatric bladder

Yngve Birkelund[Member, IEEE],
Department of Physics and Technology, University of Tromsø, Tromsø, Norway

Øystein Klemetsen[Member, IEEE],
Department of Physics and Technology, University of Tromsø, Tromsø, Norway

Svein K. Jacobsen[Senior Member, IEEE],
Department of Physics and Technology, University of Tromsø, Tromsø, Norway

Kavitha Arunachalam[Member, IEEE],
Radiation Oncology Department, Duke University, Durham, NC. She is currently with Department of Engineering Design, Indian Institute of Technology, Madras, India

Paolo Maccarini[Member, IEEE], and
Radiation Oncology Department, Duke University, Durham, NC.

Paul R. Stauffer[Member, IEEE]
Radiation Oncology Department, Duke University, Durham, NC

Abstract

We have investigated the use of microwave heating and radiometry to safely heat urine inside a pediatric bladder. The medical application for this research is to create a safe and reliable method to detect vesicoureteral reflux, a pediatric disorder, where urine flow is reversed and flows from the bladder back up into the kidney.

Using fat and muscle tissue models, we have performed both experimental and numerical simulations of a pediatric bladder model using planar dual concentric conductor microstrip antennas at 915 MHz for microwave heating. A planar elliptical antenna connected to a 500 MHz bandwidth microwave radiometer centered at 3.5 GHz was used for non-invasive temperature measurement inside tissue. Temperatures were measured in the phantom models at points during the experiment with implanted fiberoptic sensors, and 2D distributions in cut planes at depth in the phantom with an infrared camera at the end of the experiment.

Cycling between 20 second with 20 Watts power for heating, and 10 seconds without power to allow for undisturbed microwave radiometry measurements, the experimental results show that the target tissue temperature inside the phantom increases fast and that the radiometer provides useful measurements of spatially averaged temperature of the illuminated volume. The presented numerical and experimental results show excellent concordance, which confirms that the proposed system for microwave heating and radiometry is applicable for safe and reliable heating of pediatric bladder.

Index Terms

Microwave heating; radiometry; microwave antennas; hyperthermia; tissue-equivalent phantom; vesicoureteral reflux

I. Introduction

Microwave heating has been proposed and applied in hyperthermia treatment as e.g. heating of recurrent breast cancer [1], [2]. Cancerous tissue is more prone to cell death when heated compared to healthy cells, but hyperthermia is most often given in combination with radiation or chemotherapy where it can significantly improve the treatment outcome [3]. Microwave applicators range from large waveguides [4] to conformal array configurations [5]–[8], where the former variant typically is used for well-collimated deeper penetration while the latter in general performs better for larger areas of superficial tissue. The effectiveness of hyperthermia treatments is closely related to the applied thermal dose, typically in the range of 41–45°C for 60 minutes. Thermal dosimetry for feedback control of hyperthermia treatments is generally provided with a number of temperature probes, either invasive or on the skin surface. Also infrared thermography has been used for 2D dosimetry of skin surface distributions [9] and magnetic resonance imaging [10]–[12] and microwave radiometry [6], [13] are under investigation for temperature monitoring of 3D volumes at depth in the body.

Vesicoureteral reflux (VUR) is a pediatric urinary tract disorder that allows flow of urine from the bladder back up the ureters and into the kidney. Primary VUR occurs when a child is born with an impaired valve for blocking the urine to reflux from bladder to kidneys, and secondary VUR can occur when there is a blockage that hinders the normal urine flow. For both situations, infection is the most common symptom of this disease, but for secondary VUR infections may also be the cause of the urine reflux. Imaging techniques such as ultrasound imaging may be used to diagnose certain bladder and kidney abnormalities, but cannot reveal important ureter valve function with sufficient accuracy. Functional imaging techniques such as e.g. voiding cystourethrography, requires a catheter into the bladder and ionizing radiation [14], [15]. These techniques are invasive and should be avoided especially in children.

A new non-invasive method for primary VUR detection was conceptually presented by the authors in [16]–[18]. The concept is based on heating of the pediatric bladder and radiometric measurement of temperature rise in the kidney. Preliminary results using animal experiments are promising [19], [20]. In this paper, we investigate the task of heating a pediatric bladder safely using microwaves for both heating and radiometry.

The paper is organized as follows: In Section II we present the microwave theory and background related to the pediatric bladder application, in Section III we present numerical and experimental results for microwave heating and radiometry, in Section IV we discuss our findings before we conclude our paper in Section V.

II. Methodology

A. Pediatric bladder

The pediatric bladder is assumed to be filled with approximately 100 ml urine before a vesicoureteral reflux event. This corresponds to a completely filled bladder of a small child at the age 1–3 years old [17]. The placement of the bladder is in the lower abdomen, under skin and fat layers. The bladder wall is assumed to consist of a thin layer of muscle. As the microwave loss in muscle and urine is high, we can in most cases ignore the underlying internal organs in the microwave analysis.

Heating of the bladder is done using one Dual Concentric Conductor (DCC) heating antenna at 915 MHz made on two sided RO4035B laminate with thickness 1.524 mm and a

dielectric constant ε = 3.56. The DCC antenna consists of a front surface copper foil sheet with a central 25 mm square patch surrounded by a 2.5 mm gap to the surrounding ground plane while the back surface consists of microstrip feed lines connecting to the center of each side of the square patch through four vias [21]–[23]. This particular design includes a 180° phase delay in two adjoining sides of the square, resulting in an antenna with better penetration depth compared to the standard DCC due to phase addition of electric fields centrally from opposing sides of the slot radiator. A 5 mm thick water bolus is placed under the heating antennas to control the skin temperature. This technique has been applied for microwave hyperthermia treatment of breast cancer, and has been shown to be an effective approach for increasing the depth of the maximum temperature during heating [24], [25].

The chosen radiometric antenna has a microstrip feed, elliptically shaped patch on the back side and a larger elliptically shaped aperture on the front size facing the load. This particular elliptical antenna has previously been applied in ultra wideband radar applications [26] and for radiometry [27], [28] by the current authors. The radiometric antenna is placed side-by-side with the heating antenna, both angled towards the center of the bladder. Depending on the child size, their normal vectors are expected to be in the range θ = [45, 90] degrees. The conductive and convective mixing of the urine temperature inside the bladder makes the system robust against antenna placement and focus, as long as the main lobe of the antenna totally overlaps with some part of the bladder.

B. Microwave heating

The spatial distribution of heat induced with electromagnetic waves of any object strongly depends on the dielectric properties of the medium. For heterogeneous living body tissue, the spatial mix of different tissue types, varying water content and vasculature network make accurate electromagnetic and thermal simulations an almost impossible task for a specific patient.

In order to obtain some insight into the microwave heating ability of our system, we have investigated a basic setup with layered materials of heterogeneous dielectric properties close to relevant body tissues, but without any vasculature network. This allows a general investigation of the heating properties where the main limitation is that a relevant stationary heat balance cannot be obtained as the body heat source and heat sink functions are ignored. Even so, the immediate and transient heat buildup will be close to what is expected for living tissue [29].

The experiments were carried out using a heating cycle where the microwave power is turned on for a given time and then turned off for the remaining part of the cycle; a similar procedure as the one used by the current authors in animal testing of bladder heating [19], [30]. The off-time in the cycle allows time for cooling of perfused skin relative to non-perfused urine in the bladder, but most important, it provides measurement periods for the microwave radiometry without interference from microwave heating.

C. Microwave radiometry

For microwave radiometric analysis, layered tissue dielectric properties also represent a simplified model of complex heterogeneous tissue, but in this case the missing vasculature network and its convective heat transportation properties play a less important role.

For frequencies in the microwave band, the noise power from blackbody spectral radiance of a source at temperature T can be approximated by [31]

$$P = kTB \tag{1}$$

where k is the Boltzmann constant and B is the bandwidth of frequencies considered. Introducing spatial distribution of heat and dielectric properties and ignoring all frequency dependency inside the observed bandwidth, the antenna power at time t can be written as

$$P_A(t) = kB \int_V W(x, y, z) T(t, x, y, z) dV \qquad (2)$$

where $T(t, x, y, z)$ is the spatial temperature distribution at time t and $W(x, y, z)$ is a weighting function depending on a combination of antenna efficiency, the dielectric properties and the mass of illuminated tissue (or load) and the electric fields from the antenna. From the reciprocity theorem, the weighting function can also be found from the SAR or power deposition pattern of the antenna for specific loads. Note that a similar formulation using the brightness temperature T_B can be found in [32], where also system noise and external interference are included.

The microwave radiation from the human body has extremely low power levels. It is thus crucial to have a stable and sensitive radiometer to be able to detect the small variations from temperature differences of 1°C or lower. In our investigation, we have used the Dicke radiometer presented by the current authors in [28], in which the Dicke switch in front is used to protect the low noise amplifiers in the radiometer from high power microwave heating signals.

The antenna brightness temperature is calculated from the antenna power $P_A(t)$ using a linear interpolation,

$$T_B(t) = (P_A(t) - P_c) \frac{T_h - T_c}{P_h - P_c} + T_c, \qquad (3)$$

where P_h and P_c are the measured power with a hot and cold load of known temperatures, T_h and T_c, respectively.

The raw data measurements consist of alternating readings of noise power from the antenna and 50Ω reference load, at a rate of approximately 40 samples per second. The Dicke method used the measurement from the 50Ω load to correct for systematic gain variations in low noise amplifiers of the radiometer [33], giving an effective sampling rate of approximately 20 samples per second.

For each 10s time slot without microwave heating, the median value of the Dicke adjusted radiometric measurement is used to calculate the antenna brightness temperature $T_B(t)$. To investigate the variance of this antenna brightness temperature estimate, we have taken 1000 bootstrapped medians using resampling with replacement of the original data and calculated the standard deviation [34].

D. Phantom models

To evaluate the microwave heating and radiometric performance in this medical application, we have investigated an experimental setup with solid phantoms based on [35]. A low permittivity phantom that simulates fat was fabricated, consisting of 55% Ethanediol (glycol), 5% Gelatine, 40% Polythene powder (EPG), and a drop of detergent to make the mixing easier. A muscle tissue-equivalent phantom was fabricated similarly, with 48% Ethanediol, 40% Water, 2% Salt/NaCl and 10% Gelatine (EWSG). These phantoms where chosen partly because of their dielectric and thermal properties which closely resemble that of fat and muscle, as summarized in Table I, but also for their ease in cutting and shaping which facilitates thermal evaluation of the layered phantom using an infrared camera.

As the main focus of this study involved numerical and experimental verification of the combined system performance, we decided to use the muscle phantom also for mimicking the urine content in the bladder. Urine has a real permittivity close to that of DI water, but the dielectric loss is approximately twice as high as muscle tissue [18]. This leads to more power deposited and radiating in microwave heating and radiometry, respectively. The simplification using muscle tissue throughout the phantom model thus represents a worst case scenario in terms of illuminated bladder target.

Layout of the solid phantom model is shown in the left plot of Fig. 1a. This model consists of ESWG muscle phantom in the middle with a total size of $100 \times 100 \times 90$ mm^3. The ESWG phantom is cut in the middle to allow for rapid separation in order to make a horizontal plane temperature measurement at depth in phantom with the infrared camera. The picture shows the lower part of the muscle phantom together with the fat layers split apart to the side and fiber optic temperature probes for correlation with the 2D distribution measured by the infrared camera 1.

The two EPG fat layers, with sizes $85 \times 60 \times 5$ mm^3 and $60 \times 60 \times 5$ mm^3, are positioned at one corner of the muscle phantom so that the two layers are perpendicular, giving an angle θ =90° between the antennas, as shown in the numerical model in Fig. 1b. The thickness of the fat a layer is a very important parameter for the specific absorption rate (SAR) of the antennas, but the length and width do not change antenna performance as long as the antenna ground plane is smaller than these layers.

Fiber optic temperature probes2 were placed at the interface between the fat and muscle layers in the center underneath both the radiometric and heating antenna, in addition to one probe positioned approximately 15 mm from the corner in the horizontal cut plane between the two blocks of muscle phantom.

The water bolus is placed between the fat layer and the microwave heating antenna, and a constant temperature at the water bolus inlet is obtained using a closed loop fluid system with peristaltic pump, air trap and a heat exchanger in a temperature controlled water bath. An overview of the experimental setup is shown in Fig. 1c.

E. Numerical simulations

Extensive numerical simulations were carried out to provide more details and validate the conclusions of our microwave heating and radiometry model experiment. These simulations were carried out using the following commercial software: CST Microwave Studio3 for electromagnetic waves and SAR calculations, Comsol Multiphysics4 for temperature analysis, and Matlab5 for signal/temperature inversion and the final preparation of results.

A numerical model with the same dimensions as the experimental model was built in CST Microwave Studio. Standard material properties where used for copper (annealed) and distilled water, while the PCB laminates of the antennas were specified using parameters from the supplier (RO4350B). For the EPG and EWSG phantom, we imported measurements of dielectric properties taken with a commercial dielectric probe and a network analyzer6. The measured dielectric properties were taken at a temperature $T =$ 20°C, and they were assumed to be independent of temperature changes in the numerical

---

model. The resulting numerical model is shown in Fig. 1b. The water bolus under the heating antenna is set to have a uniform flow in positive x-direction, with a constant water temperature along the inlet surface.

The specific absorption rate (SAR) distributions for both antennas were calculated from the numerical simulation. The SAR results from the DCC antenna were used in temperature simulations with the same on/off heating cycles as in the experimental setup, and resulting spatial temperature distributions were used to calculate the numerical radiometric signal resulting from the SAR of the elliptical antenna from Eq. (2).

III. Results

A. Phantoms

The measured dielectric properties of distilled (DI) water, EGP and EWSG are shown as a function of frequency in Fig. 2, as a solid, dotted and dashed lines, respectively. The thick lines are the real part of the permittivity, or the dielectric constant, $\mathcal{R}e[\varepsilon]$, while the thin lines show the conductivity σ. DI water has a high dielectric constant close to 80, and an increasing loss from approximately 0.2 to 3.7 S/m in this frequency range. The EGP fat phantom has a low dielectric constant close to 5 and low loss, while the EWSG muscle phantom has an almost linearly falling $\mathcal{R}e[\varepsilon]$ from 50 to 30 in this frequency range with a significantly higher loss than both EGP and DI water.

B. Antennas

The specific absorption rate (SAR) for the DCC antenna obtained from simulation and experiment is shown in upper and lower row of Fig. 3, respectively. The level is normalized according to the highest value in the results, and contour lines correspond to dB values of −20, −16, −13, −10, −6, and −3 dB going from white to black color. SAR results for the DCC and elliptical antennas are verified experimentally using a large scantank filled with liquid muscle phantom exclusively, and a similar layout is used for the numerical simulations. The coordinate system of the results are then mapped to the experimental antenna setup shown in the right part of Fig. 1. Note that the use of a large muscle phantom/model only applies to the results in this antenna SAR section, and not to the full experimental and numerical model in the later sections.

The upper left plot in Fig. 3 shows the SAR level of the DCC antenna at position $y = −45$ mm, that is, after passing through the water bolus and fat layer, and 5 mm into the muscle phantom. The 180 degree phase delay in the DCC feed lines at two adjacent sides of square slot aperture creates a strong effective electromagnetic field in the two opposite corners located at $(x, z) = (−35, 15)$ mm and $(−5, −15)$ mm, respectively, producing the diagonally orientated elliptical shaped black (−3 dB) region. Further into the tissue, shown in the upper row of Fig. 3, the numerical results clearly show a reduction in size of the SAR pattern and a trend towards more circularly shaped central heating region. The conductivity of this phantom at $f = 915$ MHz is $\sigma = 1$ S/m, giving a skin depth for plane waves close to 16 mm. This corresponds well within an attenuation of approximately −3 dB/cm from the black −3 dB contour at $y = −45$ mm to the brighter −6 dB contour at $y = −35$ mm, shown in upper first and third plot from left in Fig. 3, respectively.

The measured SAR of the DCC antenna is shown in the lower plots of Fig. 3. The contour shapes for lower levels are typically less smooth than the numerical results, but the −3 and −6 dB contour lines shows approximately the same attenuation levels. The diagonally oriented heating pattern is pronounced at all depths in the measured results, more than observed in the numerical SAR results.

Numerical SAR results from the elliptical antenna are shown in the upper row of Fig. 4. In the upper left plot of Fig. 4, the dark −3 dB SAR contour level at position $x = -45$ mm has an almost circular shape. This SAR result is after passing through the fat layer and 5 mm into the muscle tissue, and further into the muscle tissue the level is clearly damped, as shown in the upper row of Fig. 4. At $x = -35$ mm, only the −16 and −20 dB levels are visible, which corresponds well to the higher loss, and correspondingly shorter skin depth, in muscle tissue at $f = 3.5$ GHz. The experimental results, shown in the lower row of Fig. 4, are close to the numerical results with two exceptions: The SAR at $x = -45$ mm have some irregularities in the low level dB contours, and the SAR level appears slightly less damped in the experimentally obtained results.

In Fig. 5, we show the measured S-parameters for the two antenna system consisting of the elliptical and DCC antennas. The reflection coefficient of the elliptical antenna, S_{11} shown as a solid line, has a minimum of approximately −17 dB at $f = 2.7$ GHz. However, this is a wideband antenna with $S_{11} < -10$ dB for 2.3 GHz $< f <$ 4 GHz. The DCC antenna reflection coefficient S_{22}, shown as a dashed line, has several resonances, e.g. around $f = 1.1$, 2.0, 2.6 and 3.5 GHz. At the specific heating frequency, $f = 915$ MHz, we find that $S_{22} \simeq -8$ for this experiment. The transmission coefficient between the two antennas, S_{12} shown as dashed-dotted lines, is approximately −40 dB below 1.5 GHz, and the damping between the antennas is greater than 60 dB in radiometer frequency range, 3.25 GHz $< f <$ 3.75 GHz.

C. Heating experiment

The Luxtron probe temperature measurements obtained during the heating of the phantom model are shown in Fig. 6a. The microwave heating starts at $t = 30$s, and the probe in the fat/muscle interface under the DCC antenna (marked with TX and with a dashed line) shows a rapid increase in temperature from approximately 17.5 to 28°C during the 13 heating cycles ending at $t = 420$s. At the end of each 30 second cycle, the 10 seconds with no power is also visible as the temperature rises more slowly or even decreases. The temperature in the fat/muscle interface under the radiometric antenna, marked with RX and shown as a dashed-dotted line in Fig. 6a, is almost constant just below 21°C during the whole experiment. The temperature inside the muscle phantom falls between the TX/RX probes, and shows an increase in temperature from 18 to 26.5°C.

The in-depth temperatures of the fat and muscle phantoms are taken approximately 2 minutes after the final heating cycles, and the temperature results are shown in Fig. 6b. Note that the placement of these cut planes are located under the heating and radiometric antennas, as indicated by the dark box in Fig. 1b and the dotted lines in Fig. 1c. The $z = 0$ layer shows that the temperature is above 27°C in the elliptical region bounded by −37 mm$<$ $x < -25$ mm and −42 mm$<$ $y < -34$ mm. From this heated region, the temperature drops to approximately 21°C both towards the $x = -50$ mm and $y = -50$ mm borders. Under the heating antenna, at the $y = -50$ mm surface, we find an elevated temperature in one of the corner of the antenna, but most of this surface is cooled by the cold water bolus to $\simeq$ 18°C. Under the radiometric antenna, at the $x = -50$ mm surface, we do not observe any heated regions.

In Fig. 6c, we have shown the temperatures in the numerical simulation of the solid model, located at (−20,−50, 0), (−50,−35, 0) and (−35,−35, 0) mm, respectively. These locations are at approximately the same points as described in the experimental setup shown in Fig. 6a. For the numerical results, the on/off microwave power in the heating cycles are easily identifiable for both the intersection between fat and muscle under the heating antenna and inside the muscle phantom, shown as dashed and solid lines in Fig. 6c, respectively. The corresponding temperature elevations are 17–29°C (experiment) and 19–27.5°C

(simulation). Finally, under the radiometric antenna we find a small increase in temperature from 20 to 20.5°C during the full heating experiment, from thermal conduction.

The muscle surface temperature at $t = 540$s, two minutes after the last heating cycle in the numerical simulation, is shown in Fig. 6d. The region above 27°C at the $z = 0$ mm surface is elliptically shaped and bounded by $x \in [-34,-24]$ mm and $y \in [45,-37]$ mm. Compared to the experimental results in Fig. 6b, the high temperature area seems more compressed towards the $y = -50$ mm border. We find the highest temperatures on the $y = -50$ mm cut-plane located beneath one corner of the DCC antenna, a similar position as seen for SAR for this antenna in Fig. 3. At the $x = -50$ mm muscle surface, we find a smooth transition of temperature from a central hot region around $y = -35$ mm, near where the radiometric antenna center is placed, to the corner of the muscle phantom where the inlet of the cooling water bolus is located.

D. Radiometric temperature

Figure 7a shows the radiometric results during heating of the solid phantom model. The maximum sampling rate of the power meter reading the radiometer output is $\Delta t = (1/200)$s, but reading the 50Ω load in the Dicke radiometer and limitation in the supporting software brings the effective sample rate down to approximately 1/20s. During microwave heating, as the Dicke switch is temporarily locked to the 50Ω load to protect the sensitive input, the power output jumps well above the −33.65 dBm level and the heating intervals (with no radiometric readings) are clearly visible. The in-between 10 second radiometric raw data readings have large variation, but it is still possible to identify the small increase in average power which is proportional to rise in phantom temperature.

In Fig. 7b we have shown the antenna brightness temperature after calibration of the radiometer using hot (25.5°C) and cold (1.7°C) loads. The loads in the calibration measurements were identical to the radiometer setup, using the elliptical antenna and temperature stabilized fat and muscle layers. The median result during the 20s radiometric reading periods are shown as a filled black circle, while the vertical solid lines show the estimated standard deviation. The radiometer antenna brightness temperature starts at 19.5°C and is clearly seen to increase about 1.5°C during the experiment, even though the individual radiometric reading periods show some variation. Finally, the squares in Fig. 7b show antenna brightness temperature using Eq. (3) and the numerical simulation of this heating experiment. These results show an almost linear increase in temperature during the experiment from approximately 19.5°C to 21°C as would be expected from constant applied power from the heating antenna.

IV. Discussion

The fat and muscle phantoms, EPG and EWSG, respectively, have dielectric properties close to what is expected for human tissue at $f = 1$ GHz [35]. A wide frequency range is needed for microwave heating and radiometry. The results in Fig. 2 can be compared to several measurement results from human tissue in the literature [36]–[38]. The EPG has a low dielectric constant ($Re[\varepsilon]$) and low loss (σ) for $f \in [0.8 – 4]$ GHz, in accordance with reports in the literature for fat and low water content tissue, but the linearly decreasing $Re[\varepsilon]$ and increasing σ are significantly steeper for the EWSG phantom compared to results from human muscle tissue. This discrepancy may influence the radiometric measurements, but the change to a more clinically realistic urine filled pediatric bladder will produce an even larger change in dielectric properties than this small difference between real muscle and EWSG phantom. In addition, both body tissues and phantoms have temperature dependent dielectric properties. The temperature dependency in body tissues is typically in the range +/−2% per degrees Celsius [?]. Simulations results (not shown) indicate that the effect of this would be

limited to a small displacement in the heated region, and that the antenna brightness temperature is in practice unaffected.

Using the reciprocity theorem of antennas which states that the power deposited in the tissue from a radiating antenna is identical to the spatial distribution of the received power from the radiating tissue in the antenna for a radiometric setup, we find that the elliptical antenna is well suited for this application. The S_{11} results in Fig. 5 show that the antenna is wideband, and the SAR results in Fig. 4 show that the experimental antenna reaches deeper into the muscle tissue compared to the numerical simulations. The 180° delay in feeding adjacent sides of the DCC antenna creates an elliptical shape in the heating pattern oriented diagonally across the square slot aperture. Numerically and experimentally obtained results of SAR and temperature patterns show that this antenna can be used to heat at moderate depths in the body.

The DCC antenna has a quite high reflection coefficient at $f = 915$ MHz, but the S_{11} drops rapidly and it has a clear resonance just above 1 GHz. The current DCC antenna design is based on experience in hyperthermia of recurrent breast cancer where mostly muscle tissue is expected, and where lower reflection coefficients have been observed [23]. The introduction of a fat layer in our VUR application does increase the resonance frequency of this DCC antenna, but an optimized antenna can clearly be obtained through small modifications of this design.

In the experimental model, both the muscle and the fat phantoms are initially at room temperature (20°C), and the cold water circulation in the water bolus cools down the phantoms locally before the microwave heating experiment starts. This can easily be identified as lower temperatures measured by the Luxtron fiber optic sensor under the DCC heating antenna compared to the one under the elliptical radiometric antenna. Also the sensor inside the muscle phantom shows a lower temperature than room temperature.

During the heating, the observed temperature increase in the experimental setup strongly agrees with the numerical results. The results show an increase of 1.5°C of the antenna brightness temperature during the heating experiment. The antenna brightness temperature is the effective temperature increase in the total volume sensed by the antenna, spatially weighted by the specific absorption rate distribution such that the largest contribution to the antenna brightness temperature comes from fat and muscle tissue close to the antenna. Since the experimental temperature measurement shows an insignificant temperature increase at the fat/muscle interface, we conclude that the radiometric antenna brightness temperature is sensitive to the internal temperature increase inside the muscle phantom.

The final temperature results taken with the infrared camera show some discrepancy from the numerical results. The heating pattern in the experimental results has its maximum temperature deeper into the muscle tissue, and the heat is more concentrated at depth leading to reduced temperature rise in the fat layer near the radiometric antenna. Preliminary results from animal testing of this heating system [30], showed that the urine inside the bladder had almost the same temperature. This is a result of natural convection in the bladder urine which effectively mixes heated liquid inside the bladder. In addition, the blood perfusion in biological tissues will reduce the temperature build up from microwave heating by dissipating the heat in the body. Numerical simulations using bio-heat equations for fat and muscle tissue, following the method in [25], have shown a reduction of the maximum temperature in the model by approximately 1°C. The bio-heat equations would be less important for a pediatric bladder, as the urine inside the bladder will act as a heat reservoir providing a stable temperature while the cooling effect from blood flow only interferes through heat convection at bladder walls. This differential buildup of heat in stagnant non-

perfused urine inside the bladder compared to its surrounding tissue is magnified by the 10s power-off intervals.

The observed radiometric signal during heating of the solid phantom model has large variance, but the measurements clearly follow the numerically simulated antenna brightness temperature. These results are promising and show that microwave heating and radiometry, as well as the chosen antennas and radiometer setup, are suitable for this application. The heating pattern inside this solid phantom result in a challenging radiometric setup where the warmest tissue is far from the elliptical antenna, but introduction of natural convection will distribute the temperature inside the bladder creating an almost constant temperature inside this volume. This leads to a larger volume with constant temperature close to the radiometric antenna, which increases the antenna brightness temperature compared to our solid phantom experiment.

The antenna brightness temperature $T_B(t)$ is a volumetric measure of the temperature seen by the antenna, as described in Eq. (3), but the maximum temperatures during microwave heating may be found by comparing with numerical modeling results. Temperature inversion methods using a single band radiometry and a priori knowledge of tissue parameters can also be used to estimate the urine temperature inside the pediatric bladder, following the method in [6], and multiband radiometric measurements may improve this temperature estimate [32], [39].

The main limitation in the current prototype of the radiometer is the detector circuit, which in our case consists of a software controlled Dicke switch followed by a power meter that needs to read each sample of the alternating antenna and 50Ω load (reference temperature). A crude statistical analysis based on the sampling interval internally in the power meter vs. the sampling inherent with the controlling software (1/200s and 1/40s respectively), tells us that we can expect approximately five times lower variance in the radiometric readings using an analog detection circuit with synchronized switching in this Dicke radiometer.

V. Conclusion

We have shown that the proposed microwave radiometer can do deep tissue temperature reading during microwave hyperthermia by modulating the heating power and performing the radiometric measurement during the off-period. The sensitive low-noise amplifiers in the radiometer need to be protected during the microwave heating, which can be solved by setting the Dicke switch on the radiometer front end to a 50Ω reference load.

The results from a microwave heating system using 20 W from a single conformal DCC antenna at 915 MHz show that temperature inside a multi-layer tissue phantom increases rapidly at depth, while cooling from the water bolus keeps the phantom surface less hot. The experimental and numerical results are in strong agreement, and shows that this microwave heating system is well suited for the task of heating of pediatric bladder located approximately 8 mm depth below the skin.

The proposed dual heating and radiometric monitoring approach appear well-suited for the intended clinical application in pediatric VUR detection.

Further research should include an analog detection circuit to reduce the variability and increase the sensitivity of the radiometer. The proposed dual heating and radiometric system should also be investigated for other medical applications, as e.g. monitoring and control of superficial hyperthermia treatment.

Acknowledgments

References

1. Overgaard J, Bentzen SM, Overgaard J, Gonzalez DG, Hulshof MCCM, Arcangeli G, Dahl O, Mella O. Randomised trial of hyperthermia as adjuvant to radiotherapy for recurrent or metastatic malignant melanoma. The Lancet. 1995; vol. 345(no. 8949):540–543.

2. Sugahara T, Van Der Zee J, Kampinga HH, Vujaskovic Z, Kondo M, Ohnishi T, Li G, Park HJ, Leeper DB, Ostapenko V, Repasky EA, Watanabe M, Song CW. Kadota fund international forum 2004. Application of thermal stress for the improvement of health, 15–18 June 2004, Awaji Yumebutai international conference center, Awaji island, Hyogo, Japan. Final report. Int. J. Hyperthermia. vol. 24(no. 2):p123–p140. 20080301.

3. Issels R. Hyperthermia combined with chemotherapy - biological rationale, clinical application, and results. Onkologie. 1999; vol. 22:374–381.

4. Van Rhoon GC, Rietveld PJM, Van der Zee J. A 433 MHz lucite cone waveguide applicator for superficial hyperthermia. Int. J. Hyperthermia. 1998 Januar; vol. 14(no. 1):13–27. [PubMed: 9483443]

5. Stauffer PR, Maccarini P, Arunachalam K, Craciunescu O, Diederich C, Juang T, Rossetto F, Schlorff J, Milligan A, Hsu J, Sneed P, Vujaskovic Z. Conformal microwave array (CMA) applicators for hyperthermia of diffuse chest wall recurrence. International Journal of Hyperthermia. 2010; vol. 26(no. 7):686–698. [PubMed: 20849262]

6. Jacobsen PR, Stauffer S. Can we settle with single-band radiometric temperature monitoring during hyperthermia treatment of chestwall recurrance of breast cance using a dual-mode transceiving applicator. Physics in Medicine and Biology. 2007; vol. 52:911–928. [PubMed: 17264361]

7. Lamaitret G, Dijk JDPV, Gelvich EA, Wiersma J, Schneider CJ. Sar characteristics of three types of contact flexible microstrip applicators for superficial hyperthermia. International Journal of Hyperthermia. 1996; vol. 12(no. 2):255–269.

8. Lee WM, Gelvich E, Van Der Baan P, Mazokhin V, Van Rhoon GC. Assessment of the performance characteristics of a prototype 12-element capacitive contact flexible microstrip applicator (cfma-12) for superficial hyperthermia. Int. J. Hyperthermia. 2004; vol. 20:607–624. [PubMed: 15370817]

9. Tennant A, Anderson AP. A robot-controlled microwave antenna system for uniform hyperthermia treatment of superficial tumours with arbitrary shape. International Journal of Hyeprthermia. 1990; vol. 6(no. 1):193–202.

10. Samulski TV, Clegg ST, Das S, Macfall J, Prescott DM. Application of a new techology in clinical hyperthermia. International Journal Hyperthermia. 1994; vol. 10(no. 3):389–394.

11. Gellermann J, Wlodarczyk W, Ganter H, Nadobny J, Fhling H, Seebass M, Felix R, Wust P. A practical approach to thermography in a hyperthermia/magnetic resonance hybrid system: Validation in a heterogeneous phantom. International Journal of Radiation Oncology*Biology*Physics. 2005; vol. 61(no. 1):267–277.

12. Craciunescu OI, Stauffer PR, Arabe O, Maccarini P, Das SK, Cheng K-S, Jones EL, Dewhirst MW, Vujaskovic Z. Accuracy of real time noninvasive temperature measurements using magnetic resonance thermal imaging in patients treated for high grade extremity soft tissue sarcomas. Medical Physics. 2009; vol. 36(no. 11):4848–4858. [PubMed: 19994492]

13. Ohba H, Abe K, Mizushina S, Mizoshiri S, Sugiura T. Recent Trends in Medical Microwave Radiometry. IEICE Transactions on Communications. 1995; vol. E78-B(no. 6):789–798.

14. Conway JJ, King LR, Belman AB, Thorson J, Theodore. Detection of vesicoureteral reflux with radionuclide cystography: A comparison study with roenthenographic cystography. Am. J. Roentgenol. 1972; vol. 115(no. 4):720–727.

15. Paltiel HJ, Rupich RC, Kiruluta HG. Enhanced detection of vesicoureteral reflux in infants and children with use of cyclic voiding cystourethrography. Radiology. 1992; vol. 184(no. 3):753–755. [PubMed: 1509062]

16. Snow, BW.; Stauffer, PR.; Arunachalam, K.; Maccarini, PF.; Luca, VD.; Klemetsen, O.; Birkelund, Y. Non-invasive vesicoureteral reflux detection: A new device. National Conference and Exhibition 2010, American Academy of Pediatrics; October 2–5 2010; San Francisco, CA.

17. Arunachalam K, Maccarini PF, Luca VD, Bardati F, Snow BW, Stauffer PR. Modeling the detectability of vesicoureteral reflux using microwave radiometry. Physics in Medicine and Biology. 2010; vol. 55(no. 18):5417. [PubMed: 20736499]

18. Arunachalam K, Maccarini P, De Luca V, Tognolatti P, Bardati F, Snow B, Stauffer P. Detection of vesicoureteral reflux using microwave radiometry - system characterization with tissue phantoms. Biomedical Engineering, IEEE Transactions on. 2011 june; vol. 58(no. 6):1629–1636.

19. Snow BW, Taylor MB. Non-invasive vesicoureteral reflux imaging. Journal of Pediatric Urology. 2010; vol. 6(no. 6):543–549. [PubMed: 20488755]

20. Snow B, Arunachalam K, Luca VD, Maccarini PF, Klemetsen, Birkelund Y, Pysher TJ, Stauffer PR. Non-invasive vesicoureteral reflux detection: Heating risk studies for a new device. J. Urology. 2011; vol.(no. 99) submitted.

21. Stauffer P, Rossetto F, Leencini M, Gentilli G. Radiation patterns of dual concentric conductor microstrip antennas for superficial hyperthermia. Biomedical Engineering, IEEE Transactions on. 1998 May; vol. 45(no. 5):605–613.

22. Rossetto F, Stauffer P. Effect of complex bolus-tissue load configurations on sar distributions from dual concentric conductor applicators. Biomedical Engineering, IEEE Transactions on. 1999 Nov.; vol. 46(no. 11):1310–1319.

23. Maccarini, P.; Arunachalam, K.; Martins, C.; Stauffer, P. Proc. SPIE. San Jose, CA: SPIE Press (Bellingham, WA); 2009. Size reduction and radiation pattern shaping of conformal microwave array hyperthermia applicators using multi-fed dcc slot antennas.

24. Stauffer, P.; Schlorff, J.; Taschereau, R.; Juang, T.; Neuman, D.; Maccarini, P.; Pouliot, J.; Hsu, J. Combination applicator for simultaneous heat and radiation. Engineering in Medicine and Biology Society, 2004. IEMBS '04. 26th Annual International Conference of the IEEE; 2004. p. 2514-2517.

25. Birkelund Y, Jacobsen S, Arunachalam K, Maccarini P, Stauffer PR. Flow patterns and heat convection in a rectangular water bolus for use in superficial hyperthermia. Physics in Medicine and Biology. 2009; vol. 54(no. 13):3937–3953. [PubMed: 19494426]

26. Brelum, SH. MSc thesis. University of Tromsø; 1998 August. A numerical study of planar elliptical antennas applied to ultrawideband (uwb) imaging of breast tissue.

27. Birkelund, Y.; Klemetsen, O.; Arunachalam, K.; Luca, VD.; Maccarini, PF.; Jacobsen, S.; Stauffer, PR. Radiometric temperature monitoring of microwave hyperthermia. Society For Thermal Medicine 2010 Annual Meeting; April 2010; Clearwater Beach, FL.

28. Klemetsen O, Birkelund Y, Jacobsen S, Maccarini PF, Stauffer PR. Design of medical radiometer front-end for improved performance. Progress in Electromagnetics Research B. 2011; vol. 27:289–306. [PubMed: 21779411]

29. Guy A. Analyses of electromagnetic fields induced in biological tissues by thermographic studies on equivalent phantom models. Microwave Theory and Techniques, IEEE Transactions on. 1971 Feb; vol. 19(no. 2):205–214.

30. Stauffer, PR.; Maccarini, PF.; Arunachalam, K.; Luca, VD.; Salahi, S.; Boico, A.; Klemetsen, O.; Birkelund, Y.; Jacobsen, SK.; Bardati, F.; Tognolotti, P.; Snow, B. Microwave radiometry for non-invasive detection of vesicoureteral reflux (vur) following bladder warming. Ryan, TP., editor. Vol. vol. 7901. SPIE; 2011. p. 79010V

31. Ulaby, F.; Moore, R.; Fung, A. Microwave remote sensing. Reading, MA: Addison-Wesley; 1981. vol. I: Microwave remote sensing fundamentals and radiometry.

32. Jacobsen S, Stauffer P. Nonparametric 1-d temperature restoration in lossy media using Tikhonov regularization on sparse radiometry data. Biomedical Engineering, IEEE Transactions on. 2003 Feb.; vol. 50(no. 2):178–188.

33. Dicke RH. The measurement of thermal radiation at microwave frequencies. The review of scientific instruments. 1946 July; vol. 17(no. 7):268–275. [PubMed: 20991753]

34. Efron, B. The Jackknife, the Bootstrap and Other Resampling Plans. Philadelphia, PA: Society of Industrial and Applied Mathematics; 1982.

35. Robinson MP, Richardson MJ, Green JL, Preece AW. New material for dielectric simulation of tissues. Phys. Med. Biol. 1991; vol. 36(no. 12):1565–1571. [PubMed: 1771180]

36. Gabriel C, Gabriel S, Corthout E. The dielectric properties of biological tissues: I. literature survey. Physics in Medicine and Biology. 1996; vol. 41(no. 11):2231. [PubMed: 8938024]

37. Gabriel S, Lau RW, Gabriel C. The dielectric properties of biological tissues: Ii. measurements in the frequency range 10 hz to 20 ghz. Physics in Medicine and Biology. 1996; vol. 41(no. 11):2251. [PubMed: 8938025]

38. Lazebnik M, McCartney L, Popovic D, Watkins CB, Lindstrom MJ, Harter J, Sewall S, Magliocco A, Booske JH, Okoniewski M, Hagness SC. A large-scale study of the ultrawideband microwave dielectric properties of normal breast tissue obtained from reduction surgeries. Physics in Medicine and Biology. 2007; vol. 52(no. 10):2637–2656. [PubMed: 17473342]

39. Hand JW, Van Leeuwen GMJ, Mizushina S, Van de Kamer JB, Maruyama K, Sugiura T, Azzopardi D, Edwards AD. Monitoring of deep brain temperature in infants using multi-frequency microwave radiometry and thermal modelling. Physics in Medicine and Biology. 2001; vol. 46:1885–1903.
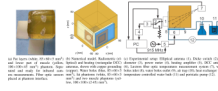
Fig. 1.
Phantom model (left), and numerical model (middle) and experimental setup (right).
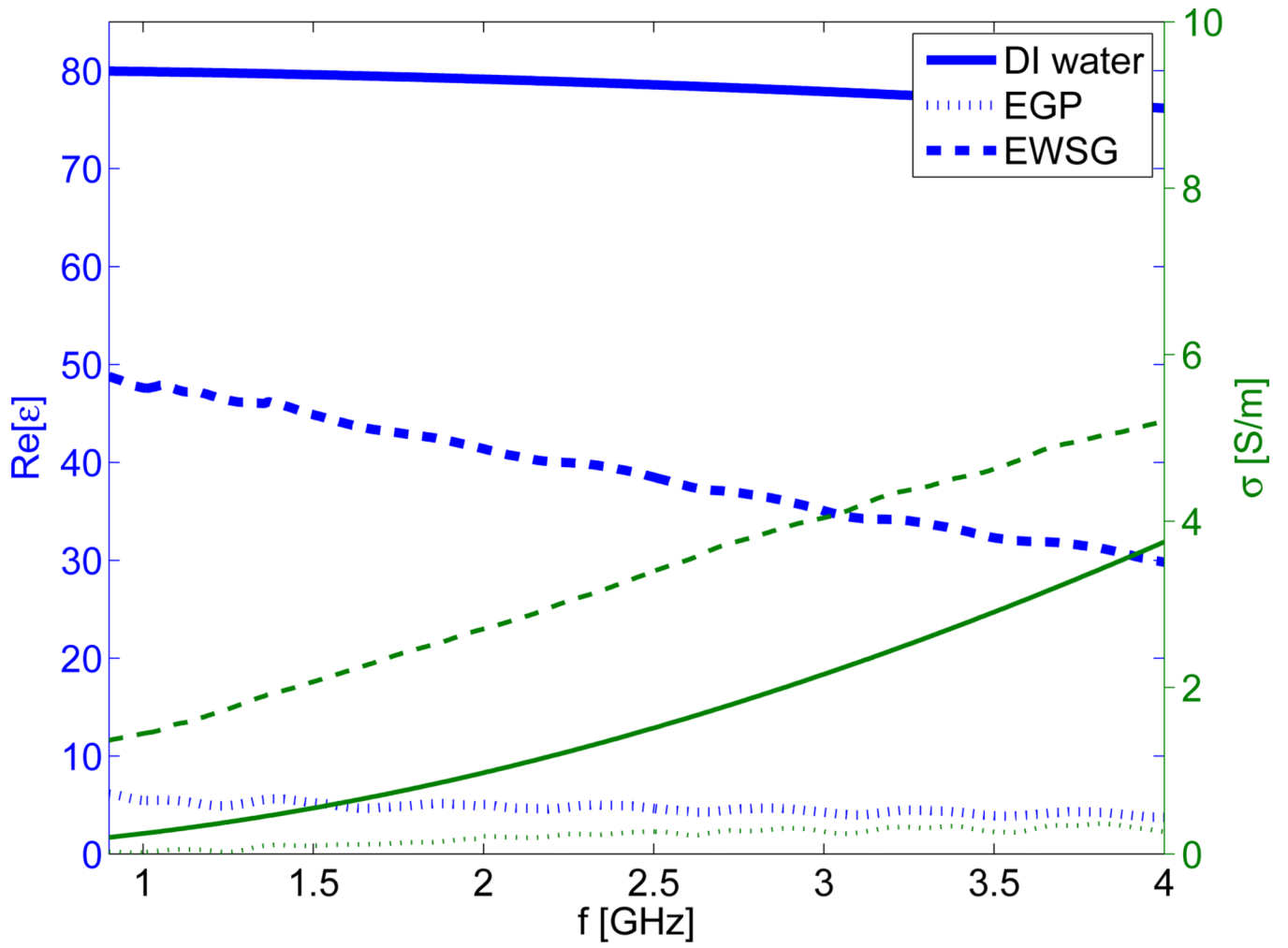
Fig. 2.
Dielectric properties of phantoms at $T = 20°C$. Dielectric constant $\mathcal{R}e[\varepsilon]$ thick (blue) lines and loss σ thin (green) lines.
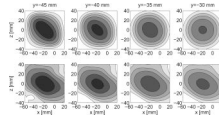
Fig. 3.
Specific absorbtion rate at four depths using a 30 mm square DCC antenna (at f = 915 MHz). Upper row: Numerical simulations. Lower row: Experimental results. Contour levels (white to black) [−20 −16 −13 −10 −6 −3] dB.
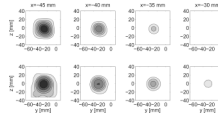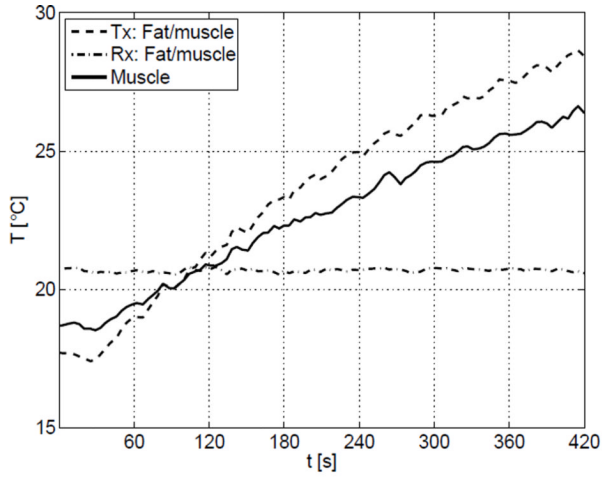
Fig. 4.
Specific absorbtion rate at four depths using elliptical antenna (at f = 3.5 GHz). Upper row: Numerical simulations. Lower row: Experimental measurements. Contour levels (white to black) [−20 −16 −13 −10 −6 −3] dB.
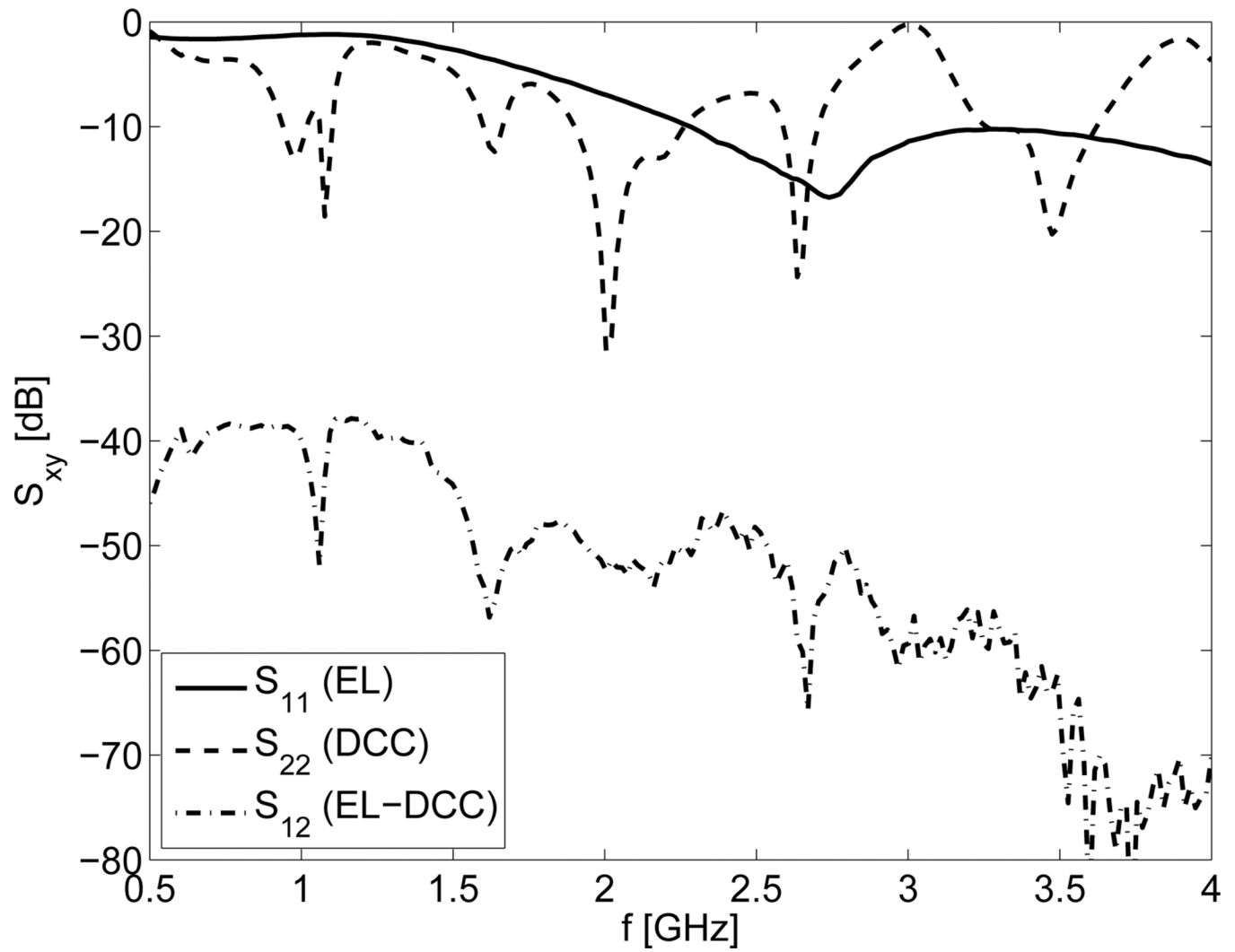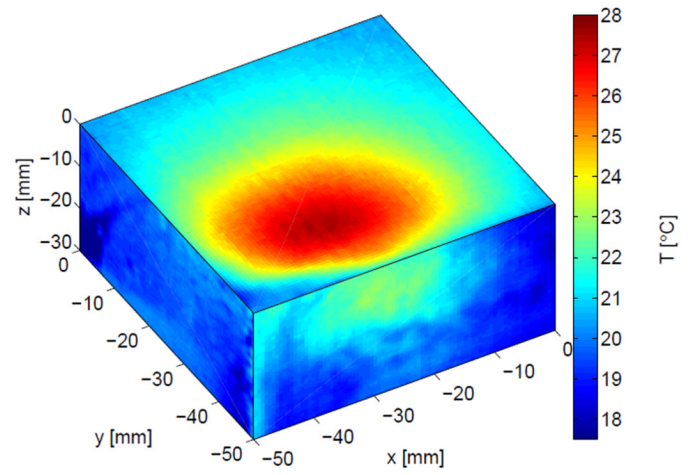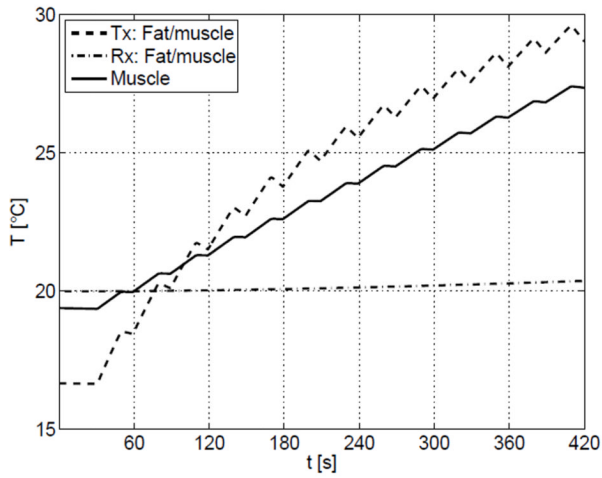
Fig. 5.
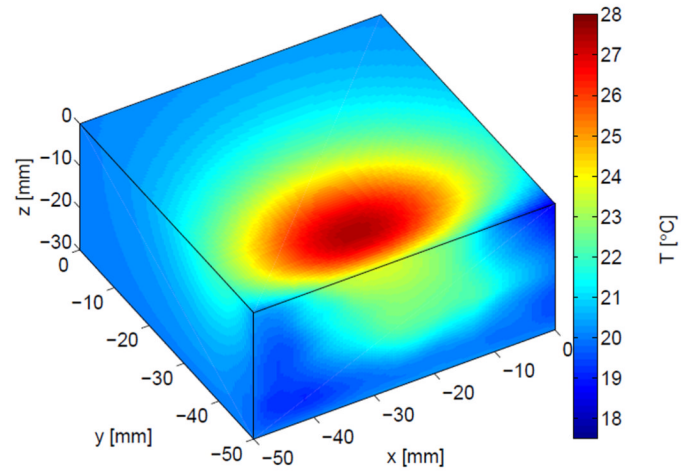Reflection and transmission coefficient.

(a) Luxtron probes.

(b) Final temperatures from infrared camera using 3 cut-planes, in-depth, of phantom.
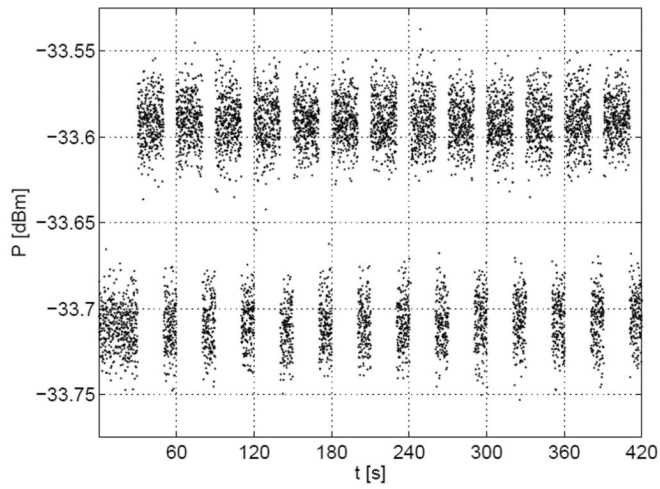

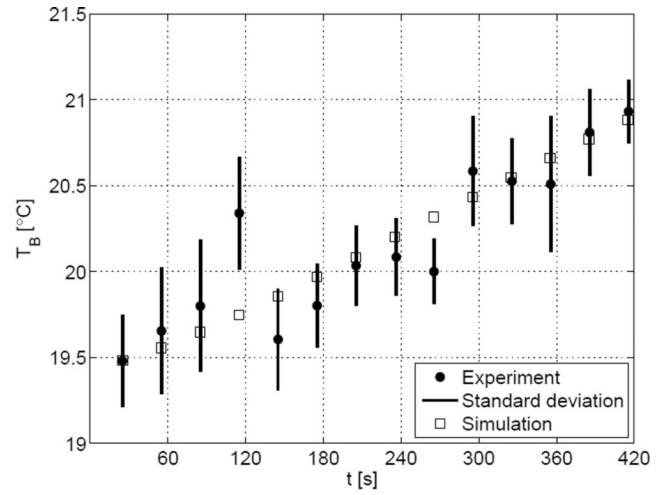
(c) Temperatures at specific positions.

(d) Same as Fig. 6b, but from simulation.

Fig. 6.
Heating of muscle phantom through water bolus and fat layers. Experimental (upper row) and simulation (lower row) temperature results.

(a) Power meter output. Upper samples: During heating, lower samples: During radiometric measurements.

(b) Antenna brightness temperature.

Fig. 7.
Radiometric temperature measurements. Raw data (left) and calibrated temperature (right).

TABLE I

Dimensional and material constants in experimental setup.

Medium	Parameter	Notation	Value
Muscle	Length	L_x	100 mm
	Length	L_y	100 mm
	Length	L_z	90 mm
Fat	Length	$L_x(L_y)$	80 mm
	Width	L_z	60 mm
	Thickness	$L_y(L_x)$	5 mm
Water bolus	Length	L_x	80 mm
	Width	L_y	60 mm
	Thickness	L_y	5 mm
	Velocity	υ	0.1 m/s
Water	Viscosity	η	0.001 sPa
	Density	ρ	1000 kg/m^3
	Specific heat	c	4200 J/kg °C
	Thermal conductivity	k	0.60 W/m °C
	Heat flux (water)	h	4 W/m^2 °C
Muscle phantom (ESWG)	Density	ρ	1100 kg/m^3
	Specific heat	c	3070 J/kg °C
	Thermal conductivity	k	0.43 W/m °C
Fat phantom (EPG)	Density	ρ	950 kg/m^3
	Specific heat	c	2250 J/Kg °C
	Thermal conductivity	k	0.29 W/m °C